

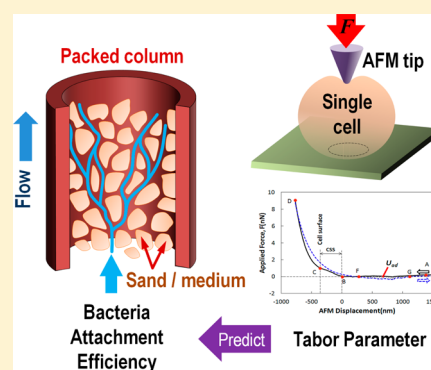
# Universal Quantifier Derived from AFM Analysis Links Cellular Mechanical Properties and Cell–Surface Integration Forces with Microbial Deposition and Transport Behavior

Yueyun Li,<sup>†</sup> Xin Wang,<sup>‡</sup> Annalisa Onnis-Hayden,<sup>†</sup> Kai-tak Wan,<sup>‡</sup> and April Z. Gu<sup>\*,†</sup>

<sup>†</sup>Department of Civil and Environmental Engineering and <sup>‡</sup>Department of Mechanical and Industrial Engineering, Northeastern University, Boston, Massachusetts 02115, United States

**S** Supporting Information

**ABSTRACT:** In this study, we employed AFM analysis combined with mathematical modeling for quantifying cell–surface contact mechanics and magnitude and range of cell–surface interaction forces for seven bacterial strains with a wide range of cell morphology, dimension, and surface characteristics. Comprehensive cell–surface characterization including surface charge, extracellular polymeric substance content, hydrophobicity, and cell–cell aggregation analyses were performed. Flow-through column tests were employed to determine the attachment efficiency and deposition–transport behavior of these bacterial strains. No statistically significant correlation between attachment efficiency and any single-cell surface property was identified. Single-cell characterization by atomic force microscopy (AFM) yielded the mechanical deformation and elastic modulus, penetration resistance to AFM probe penetration by cellular surface substances (CSS), range and magnitude of the repulsive–attractive intersurface forces, and geometry of each strain. We proposed and derived a universal dimensionless modified Tabor’s parameter to integrate all these properties that account for their collective behavior. Results showed that the Tabor parameter derived from AFM analysis correlated well with experimentally determined attachment efficiency ( $\alpha$ ), which therefore is able to link microscale cell–surface properties with macroscale bacterial transport behavior. Results suggested that the AFM tests performed between a single cell and a surface captured the key quantities of the interactions between the cell and the surface that dictate overall cell attachment behavior. Tabor’s parameter therefore can be potentially incorporated into the microbial transport model.



## INTRODUCTION

Microbial transport through porous media in subsurface environment is relevant to many aspects of environmental engineering, such as in situ or enhanced subsurface bioremediation,<sup>1</sup> drinking water supplies,<sup>2</sup> and filtration processes for water and wastewater treatments.<sup>3,4</sup> Microorganisms in the subsurface, either indigenous or bioaugmented, can profoundly impact the fate and transport of contaminants via transformation of the pollutants, adsorption and facilitated solute transport, or changes in hydraulic conductivity of the sediment layers.<sup>5,6</sup> In fact, the microbe itself as a contaminant is of interest, for instance, pathogenic bacteria and virus in a river bank filtration process in drinking water treatment.<sup>7</sup>

Traditionally, bacterial transportation is modeled by the classical colloid filtration theory (CFT), in which removal of microbes from the collector (e.g., sand grain) is assumed to be governed by either equilibrium adsorption or kinetic rate-controlled bacteria attachment to and detachment from the aquifer materials.<sup>8–10</sup> However, experimental observation shows discrepancies of CFT prediction in both lab and field scales, especially in particle deposition rates at high ionic concentration in the electrolyte.<sup>8,11–16</sup> A number of studies have shown the necessity of introducing the full intersurface

potential of electrostatic double layers developed at the surfaces of both the particle and the collector according to Derjaguin–Landau–Verwey–Overbeek (DLVO) theory.<sup>17–21</sup> Despite the improvement, bacterial deposition is often observed even when the estimated electrostatic repulsion between the interacting surfaces produces a seemingly insurmountable potential energy barrier.<sup>22</sup> To identify other relevant factors that potentially impact cell–surface interaction, a number of cell properties, including electrophoretic mobility and hydrophobicity,<sup>23</sup> surface charge heterogeneities,<sup>24</sup> and cell–surface extracellular polymeric substances (EPS) such as lipopolysaccharides,<sup>25</sup> have been studied in terms of their effects on microbe deposition behavior in porous media. Although some correlations between the microbial deposition rates and a single or combination of these parameters have been demonstrated, the consistency of the correlations and dominant factors seemed to vary depending on the microbes selected and the testing conditions.<sup>23,26</sup> The variation of these correlation conclusions indicates that cell–surface interaction is governed

Received: August 8, 2013

Revised: January 2, 2014

Accepted: January 2, 2014

Published: January 22, 2014

by various mechanisms and interplay of all of the above factors but not isolated to one or a few parameters.<sup>27</sup> In addition, there are still other essential factors, such as the elastic deformation energy of individual cells associated with adhesion contact, that have not yet been considered. This complexity highlights the need to obtain detailed mechanistic understanding of cell–cell and cell–surface interactions in order to improve and refine the conceptual and quantitative model development for fate and transport of microorganisms and consequently contaminants in subsurface.

Application of AFM (atomic force microscopy) for nano- and microscale characterization of the cell–surface properties have been demonstrated by others and shown promise<sup>28–31</sup> but mostly with qualitative interrogation. We recently explored the application of AFM in combination with mathematical data extraction and a modeling framework for microscale characterization of microbe cell–surface contact mechanics, interactions, and adhesion quantities.<sup>32</sup> We proposed and constructed a dimensionless parameter based on the quantities derived from AFM, referred as a modified Tabor parameter, to parametrize the essential features and interactions within the cell–surface system for predicting the relative propensity of cells to aggregate.<sup>32</sup> In this study, we employed AFM analysis combined with mathematical modeling for quantifying cell–surface contact mechanics and the magnitude and range of cell–surface interaction forces for a number of bacterial strains with a wide range of cell morphology, dimension, and surface characteristics. The results showed that the Tabor parameter derived from AFM analysis correlated well with attachment efficiency, experimentally determined, and therefore is able to link microscale cell–surface properties with macroscale bacterial transport behavior.

## MATERIAL AND METHODS

**Bacteria Strains.** Table S1, Supporting Information, summarizes the background information for the seven bacterial strains to be investigated: (i) *Desulfovibrio vulgaris*, (ii) *Shewanella oneidensis* MR-1, (iii) *Shewanella putrefaciens* CN-32, (iv) *Bacillus cereus*, (v) *Raoultella ornithinolytica*, (vi) *Aeromonas punctata*, and (vii) *Geobacter sulfurreducens*. These strains have environmental relevance related to either bioremediation or water quality.<sup>33–35</sup> *S. oneidensis* MR-1 and *S. putrefaciens* CN-32 were grown anaerobically in Luria–Bertani (LB) medium (25g/L) with 10 mM sodium fumarate (1.6g/L) as the electron acceptor and 10 mM sodium lactate as the electron donor. *D. vulgaris* cells were grown anaerobically in ATCC medium 1249, modified Baar’s medium for sulfate reducers. *G. sulfurreducens* cells were cultured at 30 °C under strict anaerobic condition in NBAF medium as described previously.<sup>36</sup> These anaerobic strains were grown in a glovebox at 30 °C (Coy Laboratory Products, Grass Lake, MI) with an atmosphere of 5% hydrogen/nitrogen balance. *B. cereus*, *R. ornithinolytica*, and *A. punctata* were grown aerobically at 37 °C in 25 g/L Luria–Bertani (LB) medium (Sigma-Aldrich, Inc., St. Louis, MO). Sample cells were grown at a relatively high temperature to promote growth rate before being harvested from stationary phase. To evaluate the potential impact of the growth stage on bacterial microscale adhesion properties and macroscale transportation kinetics, three samples from the exponential growth phase (E), the stationary growth phase (S), and 48-h-old growth (48) time of one strain, namely, *A. punctata*, were evaluated. Note that more detailed investigation of the impact of growth and environmental conditions (e.g.,

growth stage, media, temperature, and presence of toxins, etc.) on cell–surface properties and transport behavior is beyond the scope of this study and will be further evaluated.

### Bacteria Characterization and Cell Surface Properties

**Analysis. a. Cell Morphology and Dimension.** To determine cell dimensions, cells were stained with 1 μg/mL 4',6-diamidino-2-phenylindole (DAPI) for 10 min and then observed in situ by fluorescence microscopy (Zeiss, Axio Imager M1-1).<sup>37</sup> Individual cell lengths and widths were determined with the analytical software AxioVision Rel4.8 based on measurements of at least 20–30 cells for each strain.

**b. Electrophoretic Mobility and Surface Potential.** A Zetasizer Nano ZS90 (Malvern Instruments, Southborough, MA) was used to measure the electrophoretic mobility of bacteria suspensions. Surface potentials were approximated by the ξ potentials, which were calculated from the electrophoretic mobility using the Smoluchowski approximation.

**c. Bacteria Hydrophobicity.** The contact angle was measured to estimate bacteria hydrophobicity according to an established protocol.<sup>38</sup> Cells collected by centrifugation were resuspended in phosphate-buffered saline (PBS) and filtered through 0.45 μm (pore size) Millipore filters. Filters with a continuous bacteria layer were mounted on glass slides, and the contact angle of the bacteria surface in 0.1 M NaCl solution was measured with a contact angle analyzer (Phoenix 150, SEO Co. Suwon, Korea). At least 5 independent measurements were made to establish the average values.

**d. Extracellular Polymeric Substance (EPS) Analysis.** A modified base extraction method<sup>39</sup> was applied to measure the EPS in each strain. A 50 mL amount of bacteria sample was centrifuged, resuspended, and filtered to measure the concentration of total solids. In order to account for those EPS remaining in solution, 5 mL of the resuspended sample was filtered through 0.22 μm micrometer nitrocellulose filters as cell-free control. The pH of both sample and control was raised to 10.5 using 1 N NaOH, then placed on a shaker table at 350 rpm in 4 °C, and allowed to react for 3 h. Then samples were filtered through 0.22 μm micrometer nitrocellulose filters prior to measurement of protein and carbohydrates as EPS content. The total protein content was determined by the modified Lowry method using the Micro BCA Protein Assay Reagent Kit with a standard of bovine serum albumin (BSA). Analysis of carbohydrates was performed using the phenol–sulfuric acid method<sup>40</sup> with glucose as the standard.

**e. Cell–Cell Aggregation.** The macroscopic aggregation capacity of bacteria was characterized using a prescribed assay<sup>41</sup> and measured in terms of the aggregation index, AI, which ranges from 0 to 1 with larger AI values corresponding to higher aggregation tendency. In brief, 10 mL of cells was harvested in the stationary growth phase by centrifugation (11 000 × g for 10 min), washed twice with buffer solution (3 mM NaCl containing 0.5 mM CaCl<sub>2</sub>), and adjusted using the same buffer solution to a similar initial optical density, OD<sub>tot</sub> of about 0.30. The sample was exposed to a beam of laser with wavelength λ = 660 nm to measure the optical density OD using a plate reader (Synergy HT Multi-Mode, Biotech, Winooski, VT). Immediately after centrifuging at 650 × g for 2 min, the optical density of the carefully pipetted supernatant was measured again as OD<sub>s</sub>. The aggregation index is defined as

$$AI = \frac{OD_{tot} - OD_s}{OD_{tot}} \times 100\% \quad (1)$$

To estimate the average dimension of an aggregate, a protocol used in our previous work was adopted.<sup>32</sup> Cell suspension was gently dispersed on a glass slide, fast dried, and stained with 1  $\mu\text{g}/\text{mL}$  4',6-diamidino-2-phenylindole (DAPI) for 10 min. Then the settled multicell aggregates were observed in situ by fluorescent microscopy (Zeiss, Axio Imager M1-1).<sup>37,42</sup> At least 20 micrographs were taken at different locations for each sample. Figure S1a, Supporting Information, shows typical multicell aggregates identified manually. The nominal aggregate dimension of each aggregate was then estimated based on the equivalent diameter of the area that circumscribes the multicell aggregate based on microscopic images using the analytical software AxioVision Rel4.8. The equivalent aggregate diameter for a given strain was determined as the value at cumulative frequency of 50% (Figure S1b, Supporting Information). Duplicate measurements were performed for each strain. The number of single cells in each aggregation is estimated by dividing the average aggregation area by the mean single-cell area. Note that the aggregate size estimated here did not consider the 3-D dimension of the aggregate; however, we believe it is sufficient for the purpose of evaluating the correlation of aggregation trends with cellular surface properties.<sup>42</sup>

**Flow-Through Packed-Bed Column Tests for Determining Attachment Efficiency.** Ultrapure silica sand GRANUSIL 4095 (UNIMIN Corp., LeSueur, MN) with a nominal diameter of 0.289 mm was utilized as collector in the column testing, which was precleaned with 1 M NaOH for 24 h, rinsed with DI water, dried in an oven at 103 °C for 24 h, followed by drying in a 550 °C oven for 1 h before use. A suspension of bacteria was pumped through a 60 cc sterile syringe (i.d. of 2.67 cm) packed with clean silica sand to a height of 10 cm.<sup>43</sup> Standard gravimetric methods were used to determine the silica sand density (2.65 g/cm<sup>3</sup>) and a column packing porosity of 0.4. Prior to each deposition measurement the packed column was equilibrated by pumping 20 pore volumes of DI water followed by 10 pore volumes of the background electrolyte solution (3 mM KCl) through the column at a constant flow rate of 5 mL/min (filtration velocity of 0.015 cm/s). A suspension of bacteria in the same background electrolyte solution was pumped for 3–4 pore volumes, followed by pumping bacteria-free background electrolyte solution (about 3 pore volumes) at the same rate as mentioned above. A constant influent particle concentration,  $C_o$ , was maintained by including a miniature magnetic stir bar in the bacteria solution tank, and the influent particle concentration at the column inlet was measured every 1/4 of a pore volume. The bacteria concentration at the column outlet was monitored continuously using online optical density measurements (at 500 nm) with a UV-vis spectrophotometer (model UV Mini 1240 Shimadzu, Kyoto, Japan) and a 1 cm flow-through cell.

Attachment efficiency,  $\alpha$ , is defined as the ratio of experimental single-collector removal efficiency ( $\eta$ ) to the theoretical single-collector contact efficiency ( $\eta_o$ ), i.e.,  $\alpha = \eta/\eta_o$ . Values of  $\eta_o$  for each strain were determined using the expression proposed by Tufenkji and Elimelech.<sup>44,45</sup>

The single-collector removal efficiency can be determined from each breakthrough curve as follows

$$\eta = \frac{-2d_c \ln(1 - C/C_o)}{3(1 - \varepsilon)L} \quad (2)$$

where  $d_c$  is the diameter of the quartz sand,  $\varepsilon$  is the bed porosity, and  $L$  is the packed column length. The normalized column effluent concentration,  $C/C_o$ , was obtained from each breakthrough curve by averaging the values measured between pore volumes 1.8 and 2 (i.e., clean bed conditions).<sup>24</sup> Attachment efficiencies ( $\alpha_{\text{BTC}}$ ) based on the breakthrough curve are then determined as  $\alpha = \eta/\eta_o$ .

Attachment efficiency can also be calculated from the profile of retained cells,<sup>44</sup>  $S(x)$

$$S(x) = \frac{t_o \varepsilon k}{\rho_b} C(x) = \frac{t_o \varepsilon k C_o}{\rho_b} \exp\left[-\frac{k}{u} x\right] \quad (3)$$

Here  $k$  is the cell deposition rate coefficient,  $u$  the interstitial cell velocity,  $\rho_b$  the porous medium bulk density, and  $t_o$  the duration of continuous cell injection at concentration  $C_o$  (at  $x = 0$ ). The cell deposition rate coefficient,  $k$ , is related to  $\eta$  via

$$k = \frac{3(1 - \varepsilon)u}{2d_c} (\eta_o \alpha) \quad (4)$$

Linearization of eq 3 reveals that  $k$ , and thus  $\alpha$ , can be obtained from both the intercept and the slope of a semilog plot of  $S(x)$

$$\ln S(x) = \ln\left(\frac{t_o \varepsilon k C_o}{\rho_b}\right) - \frac{k}{u} x \quad (5)$$

For each experiment, the value of the attachment efficiency was calculated from the intercept ( $\alpha_{\text{int}}$ ) and slope ( $\alpha_{\text{slope}}$ ) of a semilog plot of the retained particle profile,  $S(x)$ .

**Column Dissection and Enumeration of Retained Cells on Sand.** After completing each flow-through column test the packed bed was dissected into sections to obtain the spatial distribution of particles as suggested by Tufenkji and Elimelech.<sup>44</sup> The column bottom end piece was removed, and the porous medium saturated with electrolyte solution was extruded in 1 cm wide sections by gravity. Each 1 cm section of porous media was placed into a 50 mL Falcon tube containing 5 mL of 1 mM NaOH to release the retained cells from the sand grains surface. After 1 h, representative 1 mL samples of the supernatant from each tube were withdrawn, added to a sterile 2 mL tube containing 200  $\mu\text{L}$  of 4% PFA, and used for bacterial enumeration in accordance to a published protocol,<sup>46</sup> as summarized in the Supporting Information (SI 1). The remaining sand–cell solution mixture in each tube was emptied into preweighed aluminum dishes, weighed, and placed in an oven to evaporate the remaining liquid. The mass of sand and volume of solution in each section were determined by mass balance. At least three replicates were performed with each strain.

**Atomic Force Microscopy and Derivation of the Tabor Parameter.** A 1 mL amount of a suspension of bacteria culture in 3 mM KCl solution was pipetted onto a gelatin-treated cleaved mica disk (Sigma G-6144) for AFM indentation. Force measurements were repeated on mica surfaces before and after probing the bacteria samples to ensure minimal contamination of the silicon nitride AFM tip. A typical cell was identified by large scan size and low-resolution MAC (magnetic acoustic control) mode. The AFM tip was then repositioned over the cell before switching from tapping to contact mode for indentation. Applied load,  $F$ , was measured as a function of the vertical displacement of the AFM tip,  $w$ . The mechanical response,  $F(w)$ , was obtained for loading–unloading (compression–tension) of the tip. At least five loading–unloading

cycles were performed on different areas of selected cells and at least 10–15 cells of each sample batch.

Figure 1 shows the typical force–displacement curve by AFM. When the AFM tip is still relatively far away from the cell

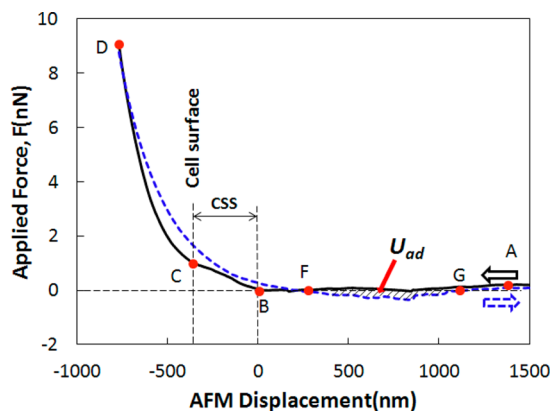


**Figure 1.** Exemplary AFM force loading (solid black line, A–B–C–D) and unloading (dotted blue line, D–F–G) curve of *Aeromonas punctata*. Thickness of the cellular surface substances (CSS) is defined as the distance from the starting point of force detection (point B) to cell surface (point C). Adhesion energy  $U_{ad}$  is defined by the shaded area of loading–unloading hysteresis, which is the total work needed to detach the AFM tip from the cell.

sample the interaction force is so weak that the measured force is set to baseline for apparent “zero” load (path AB). Upon further loading AFM will touch CSS at point B and penetrate the whole layer along path BC (see Supporting Information, SI 2, for detailed description on the determination of point C). The equilibrium thickness of CSS is defined as the length of BC, from where the AFM tip first senses the presence of intersurface forces to AFM tip touching the cell surface during loading. The AFM tip will cause global deformation to the cell along path CD, from which the cell elastic modulus is calculated.<sup>47</sup> The elastic modulus calculation method is briefly summarized in the Supporting Information (SI 3). Then the AFM tip will be retracted from the cell surface upon the unloading curve (dotted blue line), and the cell will gradually resume the original shape. When the tip is released from the cell surface it will travel back along CSS layer. The applied force will be tensile along path FG. The observed sawtooth pattern is due to sudden detachment of CSS from the AFM tip. The adhesion energy,  $U_{ad}$ , is defined by the shaded area which is the total work needed to detach the AFM tip from the cell surface or CSS layer. The spring constant of the AFM cantilever was determined by the average force curves to be  $0.205 \pm 0.015$  N/m according to the Cleveland method.<sup>48</sup> With the attempt to derive a universal dimensionless parameter to collectively combine these measurable quantities, the modified Tabor parameter,<sup>32</sup>  $\mu$ , based on classical adhesion and colloidal science was defined as

$$\mu = \left[ \frac{2b_2}{l^3 E^2} \left( \frac{U_{ad}}{\pi R_{AFM}^2} \right)^2 (1 - \nu^2)^2 \right]^{1/3} \quad (6)$$

where  $b_2$  is the width of the ellipsoidal cell determined from cell dimension measurements,  $l$  is the thickness of the cellular surface substances (CSS) measured as the length of BC (Figure 1),  $E$  is the cell elastic modulus calculated from the extent of

cell membrane deformation when a loading force was applied through the AFM tip,  $U_{ad}$  is the total adhesion energy needed to detach the AFM tip from sample cell,  $\pi R_{AFM}^2$  is the contact area of the AFM tip,  $R_{AFM}$  (10 nm) is the AFM tip radius, and  $\nu$  (0.5) is the Poisson ratio. The Tabor parameter proposed reflects the cell–surface interaction quantities as well as the cell dimension and mechanical properties (see more discussion in the Results section). A more detailed description of the basis and development of Tabor’s parameter is provided in the Supporting Information (SI 4).

## RESULTS AND DISCUSSIONS

### Diverse Transport Behavior among Bacterial Strains.

A diverse microbial transport behavior of different strains, reflected by both cell breakthrough curves (Figure 2) and cell

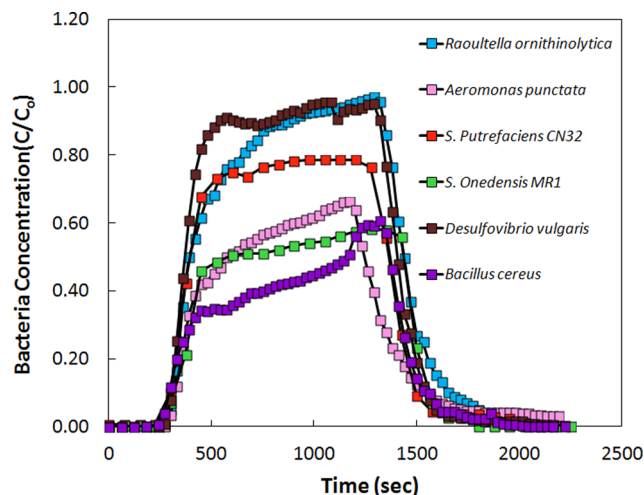


**Figure 2.** Representative breakthrough curves for *S. oneidensis* MR1, *S. putrefaciens* CN32, *D. vulgaris*, *R. ornithinolytica*, *A. punctata*, and *B. cereus* cells in columns packed with silica sand at a solution ionic strength of 3 mM KCl. Experimental conditions:  $C_0 \approx 10^8$  cells/mL, approach velocity 0.015 cm/s, porosity 0.4, mean sand diameter 0.289 mm, pH 8–8.5, and temperature 20–22 °C. All strains were from stationary growth stage.

deposition distribution patterns in media (Figure 3), was observed under the same chemical and flow condition. For example, around 20% of *R. ornithinolytica* and *D. vulgaris* cells were retained in the column ( $C/C_0$  about 0.8), whereas more than 70% of the of *B. cereus* cells were retained. It is noted that the breakthrough curves for *R. ornithinolytica*, *A. punctata*, and *B. cereus* exhibit a monotonic increasing function of time, which is widely discussed in the literature. Possible explanations include “blocking” the impact of deposited bacteria that reduces the area available for deposition,<sup>49</sup> simultaneous bacterial deposition and release,<sup>50</sup> colloid/microbial collisions that knock off weakly associated cells from the collector surface,<sup>51</sup> and a superposition of straining and attachment processes,<sup>52</sup> etc. Simultaneous cell deposition and detachment in this case is unlikely the major reason because except for *A. punctata* no obvious concentration tailing<sup>27</sup> was observed in the breakthrough curves.

Figure 3 shows the profile of retained cell concentration along the sand column length. For *R.ornithinolytica*, *A. punctata*, and *B. cereus*, significantly more cells were deposited in the beginning of the column than those retained in the end, presumably as a result of a physical straining process.<sup>52</sup>

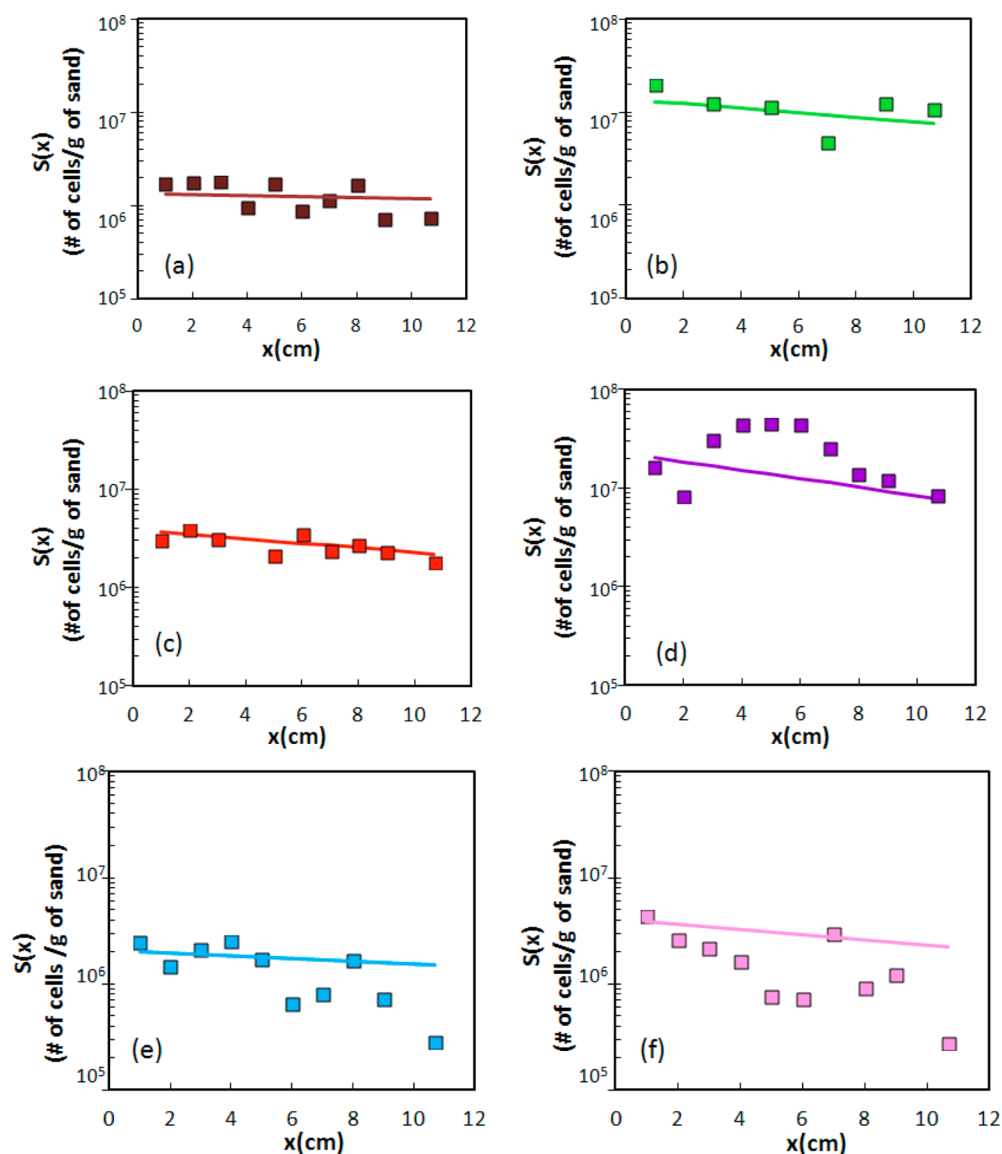


**Figure 3.** Distribution of retained bacterial cells on per gram of dry sand as a function of distance from the column inlet (symbols). Solid lines present the prediction curves for the six strains: (a) *D. vulgaris*, (b) *S. oneidensis* MRI1, (c) *S. putrefaciens* CN32, (d) *B. cereus*, (e) *R. ornithinolytica*, and (f) *A. punctata*. All strains were from stationary growth stage. Prediction curve was based on the classic CFT model as shown in eq 5, where  $k$  was determined from flow-through column tests results according to eq 3.

Significant deposition close to the inlet leads to clogging, which in turn reduces the percolation channels in the porous medium. After the first few clogging centimeters cells would be only mobile in the larger continuous pore networks, which would inhibit straining, and the number of retained cells therefore decreased.<sup>52</sup> Significant deviation of our measurements from theoretical prediction according to CFT is also noticed in Figure 3. In addition, the difference in values of  $\alpha$  calculated from either the breakthrough curve ( $\alpha_{BTC}$ ) or the slope and intercept of a semilog plot of the measured retained particle profile ( $\alpha_{slope}$  and  $\alpha_{int}$ ) were calculated (Table 1) to quantify the degree of deviation from the CFT as proposed by Tufenkji and Elimelech.<sup>44</sup> In such a comparison, the ratios of  $\alpha_{slope}/\alpha_{BTC}$  and  $\alpha_{int}/\alpha_{BTC}$  should be equal to 1, assuming perfect agreement between the observed spatial distribution of retained cells and that predicted by CFT. As shown in Table 1, the ratio varied from 0.5 to 6, suggesting a limitation of the classical CFT for predicting microbial deposition.

To further investigate the reason for the breakdown of CFT observed in this study,<sup>44</sup> DLVO theory was used to calculate the bacteria–quartz interaction energy as a function of displacement when a bacterial cell approaches the quartz collector surface using the  $\zeta$  potentials of bacteria (Table 2) and sand (details in Supporting Information SI 5).  $\zeta_{quartz}$  values were taken from Redman et al.,<sup>53</sup> as they were obtained with the same pH and ionic strength as used in this study. The DLVO surface potential reveals the presence of a significant repulsive energy barrier in the range of 208–822  $k_B T$  (Table S2, Supporting Information). Since the average thermal energy of a single bacterial cell is on the order of  $0.5k_B T$ ,<sup>54</sup> it is unlikely that they are capable of overcoming the energy barrier at ambient conditions, although the bacteria mobile (i.e., swimming) energy could potentially facilitate the cell from overcoming the energy barrier.<sup>55</sup> The secondary minimum, which was proposed in a recent study to explain the breakdown of CFT evaluation,<sup>43</sup> ranged from 0.0 to 0.38  $k_B T$ , and they are

**Table 1. Experimentally Determined Attachment Efficiencies<sup>a</sup>**

bacteria strain	$C/C_0$	attachment efficiency <sup>b</sup>			deviation ratio	
		$\alpha_{BTC}$	$\alpha_{slope}$	$\alpha_{int}$	$\alpha_{slope}/\alpha_{BTC}$	$\alpha_{int}/\alpha_{BTC}$
<i>D. vulgaris</i>	0.86	0.11	0.61	0.13	5.74	1.20
<i>S. oneidensis</i> MR-1	0.54	0.45	0.44	0.52	0.98	1.15
<i>S. putrefaciens</i> CN32	0.77	0.18	0.19	0.20	1.03	1.12
<i>B. cereus</i>	0.21	0.92	0.46	0.96	0.50	1.04
<i>R. ornithinolytica</i>	0.73	0.23	1.39	0.36	6.01	1.56
<i>G. sulfurreducens</i>	0.93	0.024	c	c	c	c
<i>A. punctata</i> S	0.47	0.56	1.53	0.45	2.75	0.81
<i>A. punctata</i> E	0.46	0.61	c	c	c	c
<i>A. punctata</i> 48	0.82	0.15	c	c	c	c

<sup>a</sup>All strains were from stationary growth state except for *A. punctata*, which is indicated by stationary (S), exponential (E), and 48 h growth (48). <sup>b</sup>Values of the single-collector contact efficiency ( $\eta_0 = 4.5 \times 10^{-3}$ ,  $1.1 \times 10^{-3}$ ,  $4.2 \times 10^{-3}$ ,  $4.1 \times 10^{-3}$ ,  $4.1 \times 10^{-3}$ ,  $4.1 \times 10^{-3}$ , and  $9.0 \times 10^{-3}$  for *D. vulgaris*, *S. odenesis* MR1, *S. putrefaciens* CN32, *B. cereus*, *R. ornithinolytica*, *A. punctata*, and *G. sulfurreducens*, respectively) were calculated with the following parameter values:  $d_c = 0.289$  mm,  $d_p$  for each strain is shown in Table 2,  $U = 1.5 \times 10^{-4}$  m/s,  $A = 6.5 \times 10^{-21}$  J,  $T = 296$  K,  $\rho_p = 1050$  kg/m<sup>3</sup>,  $\rho_f = 1000$  kg/m<sup>3</sup>,  $\mu = 1.005 \times 10^{-3}$  kg/(m s), and  $\epsilon = 0.4$ . <sup>c</sup>Not measured

too shallow to keep the kinetic cells retained under this condition. Thus, DLVO interaction, including both primary and secondary minima, determined from the current DLVO theory, is not sufficient to explain the cell deposition behavior observed in this study.

**Impact of Cell Surface Characteristics on Transport Behavior.** Table 2 summarizes the distinct cell surface characteristics of the 7 bacterial strains. All samples possess equivalent diameters ranging from 0.3 to 1.5  $\mu$ m and are all in the form of rods except *D. vulgaris* (vibrio). In this study, the contact angle, as an estimate of hydrophobicity (assuming similar porosity of bacteria layer), was found to range from 14.8° to 45.5°, such that all strains could be considered hydrophilic.<sup>56</sup> Less hydrophilic cells adhere to a greater extent compared to their hydrophilic counterparts.<sup>38</sup> No significant correlation between contact angle and attachment efficiency was observed in the present study.

A statistically sound relationship was reported between  $\zeta^{-1}$  and  $\alpha$  obtained in a column test with raw quartz particles.<sup>26</sup> This is qualitatively consistent with DLVO theory, which predicts  $\alpha$  to be higher for cells with a lower net negative charge

and thus a diminished electrostatic double-layer repulsion at the cell–sand interface.<sup>24</sup> However, other contradictory studies indicated that there was no direct correlation between deposition behavior and zeta potential.<sup>43,57</sup> In the present study, all sample strains were negatively charged with  $\zeta = -39.4$  (*G. sulfurreducens*) to  $-18.4$  mV (*S. oneidensis* MR-1) in 3 mM KCl. No statistically significant correlation was observed between  $\zeta$  and the attachment efficiency, indicating that though electrostatic double-layer repulsion (EDL) interactions might play an important role the surface charge alone, however, is not sufficient to predict bacteria deposition behavior for all seven strains investigated.

Extracellular polymeric substances (EPS), such as protein, carbohydrate, and humic acids, present on the outer cell membrane are known to result in steric repulsion that affects the cell adhesion behavior.<sup>25,58</sup> Table 2 reports the amount of the EPS in terms of milligrams per gram of total suspended solid in each strain determined by the base extraction method.<sup>39</sup> However, neither the extracted EPS protein nor carbohydrates showed any significant correlation with  $\alpha_{BTC}$  in the prescribed condition.

Bacterial aggregation is critical in studying deposition in porous media. The increased dimension of a multicell aggregate compared to an isolated cell inevitably leads to straining and even influences the aggregate–collector interaction behavior. The 7 strains in the present study exhibited a wide range of aggregation index from 0.12 to 0.75. Figure S1, Supporting Information, shows typical multicell aggregates and cumulative statistics of their diameter,  $d_a$ . A reasonable correlation between  $\alpha_{BTC}$  and  $d_a$  was observed (Pearson correlation  $r_p = 0.84$ ,  $p = 0.02$ ).

Recall that both the breakthrough curve and the retained cell profile for *R. ornithinolytica*, *A. punctata*, and *B. cereus* suggested a straining effect in their transport process through porous media. Recent studies also suggested that physical straining could play a significant role when the ratio of particle (i.e., bacterial cell) diameter to the collector (i.e., sand),  $d_p/d_c$  is greater than 0.0017.<sup>52</sup> The single-cell–collector size ratio,  $d_p/d_c$  for these 3 strains is determined to be 0.005, and the aggregate–collector size ratio,  $d_a/d_c$  is as high as 0.05. Thus, for these strains that tend to form aggregates physical straining could play a very important role in their deposition process.<sup>59</sup>

**Cell–Surface Interactions Characterization with AFM Analysis.** The elastic modulus of the cell wall under pressure and the range and magnitude of the overall adhesion forces holding the cell and silica tip together, which should be a combination of both short-ranges forces, such as van der Waals

**Table 2. Cell Surface Characteristics, Aggregation Quantification, and EPS Presence**

bacteria strain <sup>c</sup>	equivalent diameter, $d_p$ ( $\mu$ m)	contact angle (deg)	AI	equivalent aggregate diameter, $d_a$ ( $\mu$ m)	$\zeta$ potential (mV)	EPS (mg/g TSS)	
						protein	carbohydrate
<i>Desulfovibrio</i> (vibrio)	0.942 $\pm$ 0.03	45.5 $\pm$ 4.5	0.29 $\pm$ 0.07	3.0 $\pm$ 2.2	-37.1 $\pm$ 4.86	5281 $\pm$ 1048	BDL <sup>a</sup>
<i>S. oneidensis</i> (rod)	1.559 $\pm$ 0.28	30.3 $\pm$ 4.9	0.21 $\pm$ 0.04	2.2 $\pm$ 1.1	-18.4 $\pm$ 7.7	748 $\pm$ 293	185 $\pm$ 95
<i>S. putrefaciens</i> (rod)	1.197 $\pm$ 0.18	15.5 $\pm$ 4.7	0.12 $\pm$ 0.04	1.0 $\pm$ 0.4	-29.9 $\pm$ 7.4	1068 $\pm$ 288	143 $\pm$ 40
<i>Bacillus</i> (rod)	1.529 $\pm$ 0.18	29.8 $\pm$ 4.1	0.75 $\pm$ 0.12	19 $\pm$ 10	-21.5 $\pm$ 5.48	142 $\pm$ 44	31 $\pm$ 12
<i>Raoultella</i> (rod)	1.474 $\pm$ 0.15	20.1 $\pm$ 2.2	0.57 $\pm$ 0.03	4.9 $\pm$ 2.5	-33 $\pm$ 9.11	137 $\pm$ 43	108 $\pm$ 10
<i>Aeromonas</i> (rod)	1.518 $\pm$ 0.20	14.8 $\pm$ 1.7	0.60 $\pm$ 0.02	4.2 $\pm$ 2.0	-21.6 $\pm$ 4.09	307 $\pm$ 150	251 $\pm$ 19
<i>Geobacter</i> (rod)	0.314 $\pm$ 0.04	b	0.18 $\pm$ 0.01	b	-39.4 $\pm$ 5.59	b	b

<sup>a</sup>BDL: Below detection limit. <sup>b</sup>Not measured. <sup>c</sup>All strains were from stationary growth stage.

Table 3. Cell–Surface Interaction Properties Determined Based on AFM Analysis and Tabor's Parameter

bacteria strain <sup>a</sup>	adhesion energy (10 <sup>-18</sup> J)	short axis of the ellipsoidal cell (nm) <sup>b</sup>	equilibrium thickness of CSS(nm)	elastic modulus (kPa)	Tabor's parameter
<i>Desulfovibrio</i>	110.1 ± 68	593.5 ± 100	515 ± 92	102 ± 14	3.9 ± 0.3
<i>S. oneidensis</i>	536.4 ± 29	504.8 ± 70	243.5 ± 55	249 ± 31	12.3 ± 4.1
<i>S. putrefaciens</i>	126.5 ± 29	421.4 ± 70	184.0 ± 43	499 ± 30	3.7 ± 0.2
<i>Bacillus</i>	964 ± 213	734.0 ± 110	103 ± 45	211 ± 88	54.2 ± 2
<i>Raoultella</i>	211.8 ± 105	795.8 ± 300	294 ± 101	153 ± 18	8.8 ± 0.8
<i>Aeromonas S</i>	281.2 ± 72	775.2 ± 380	265.6 ± 52	105 ± 31	15.0 ± 4.6
<i>Aeromonas E</i>	53 ± 24	775.2 ± 380	81.3 ± 32.8	63.1 ± 4.1	22.6 ± 2.7
<i>Aeromonas 48</i>	26836 ± 56	775.2 ± 380	245 ± 78	375 ± 15	6.8 ± 1.1
<i>Geobacter</i>	528 ± 121	320 ± 180	132.46 ± 83	528 ± 101	4.6 ± 2.2

<sup>a</sup>All strains were from stationary growth stage, except for *A. punctata*, which is indicated by stationary (S), exponential (E), and 48 h growth (48).

<sup>b</sup>Values for short axis of the cell were determined from DAPI stained image.

and electrostatic, and long-range forces, such as those due to the presence of cellular surface substances (CSS) with varying thickness and density, could be inferred from the AFM measurement (Table 3). The results show that different bacteria strains possess different mechanic properties. *G. sulfurreducens* was determined to have the highest elastic modulus, while *D. vulgaris* had the lowest. Although compliant cells with small elastic modulus would tend to conform to one another, making the resulting multicell aggregate more resistant to segregation,<sup>32</sup> no significant correlation was found between elastic modulus and aggregation index or aggregate diameter in this study.

Adhesion energy was also found to vary greatly with strains. Although it is intuitively expected that the higher adhesion energy might result in higher cell–cell aggregation and cell–surface adhesion tendency and extent, this is not evident with our results. No significant correlation was found between adhesion energy and aggregation or deposition behavior.

The “thickness” of the extracellular cell surface substance (CSS, such as EPS or other substance that contribute to interactive force) layer ranges from 103 to 515 nm. *D. vulgaris* exhibited a significantly longer force range (presumably to be associated with a higher amount of CSS around the cell) compared to the others strains, which is in agreement with the higher level of EPS detected as shown in Table 2.

**Tabor Parameter as a Predictor for Microbial Deposition Behavior.** In classic adhesion and colloid science, when two identical solid elastic spheres of dimension  $b$  come into contact under an external compressive load,  $F$ , in the presence of intersurface forces with adhesion energy,  $U_{ad}$ , a contact circle of radius,  $c$ , is formed at the interface (as illustrated in Figure 4). A dimensionless Tabor's parameter,  $\mu = (2bU_{ad}^2/9E^2l^3)^{1/3}$ , was derived by Tabor and then Maugis<sup>60</sup> to encompass geometry ( $b$ ), interfacial properties ( $U_{ad}$ ), intersurface force range ( $l$ ), and material elasticity of the solid ( $E$ ). In physical terms,  $\mu$  governs the size of the contact area,  $c$ , at the adhesion interface as well as the deformability due to adhesion. A compliant cell, once adhered to the sand surface, would deform more drastically than a rigid cell, making it more geometrically streamlined and thus experiencing less hydrodynamic drag.<sup>61</sup> Therefore, for bacterial cell it is conceivable that large and easily deformable (compliant) cells are expected to be more prone to aggregation and adhesion, especially when the adhesive intersurface force is strong and the steric repulsion as a result of CSS thickness is minimized. In quantitative terms, a higher propensity to aggregation and adhesion is expected for large  $U_{ad}$  and  $b_2$  and small  $l$  and  $E$ . It is ideal to derive a

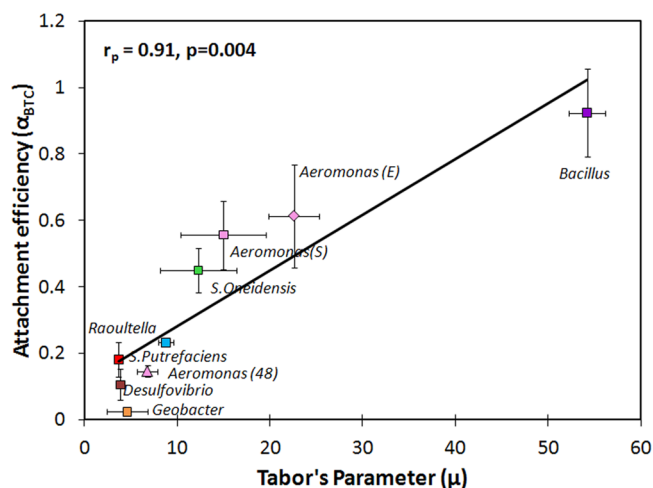


**Figure 4.** Pearson correlation between Tabor's parameter ( $\mu$ ) and attachment efficiency ( $\alpha_{BTC}$ ). Tabor's values were derived from AFM analysis that captures cell dimension, cell elasticity, range of cell–surface forces (apparent cell surface substance (CSS) thickness), and adhesion forces and energy. Attachment efficiency was determined based on the breakthrough curve, as described in Figure 1. Error bar represents the standard deviation from at least three replicates. All strains were in stationary stage. For *Aeromonas*, cells from stationary stage (S), exponential stage (E), and at 48 h are shown for comparison.

universal dimensionless parameter to collectively combine these measurable quantities.

We therefore modified the Tabor parameter<sup>60,62</sup> with AFM-measured properties to fit our needs (see eq 6). On the basis of classic adhesion and colloidal science it is anticipated that large Tabor value facilitates compliant cells to adhere. It would be therefore logically expected that a large  $\mu$  leads to a higher deposition rate in porous media. As shown in Figure 5, Tabor's parameter, which encompasses cell dimension, cell elasticity, range of cell–surface forces (CSS thickness), and adhesion forces and energy, correlated very well with the attachment efficiency ( $\alpha_{BTC}$ ) experimentally determined for all bacterial strains and growth stages studied (Pearson correlation  $r_p = 0.91$ ,  $p = 0.004$ ). In spite of the limitation of the AFM test to fully simulate the cell–sand interaction, the strong linear correlation observed for a variety of bacterial strains indicated that the Tabor parameter is a promising parameter to correlate the microscale cell properties and cell–surface interaction quantities to macroscale cell transport and deposition behavior in porous media.

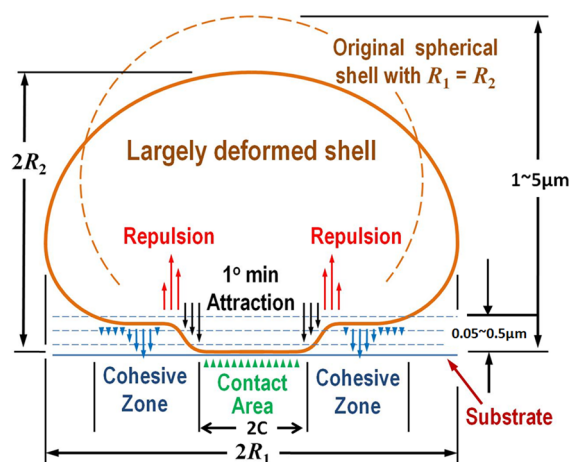


**Figure 5.** Cell deformation affects the intersurface forces between cell and collector surface. Cells with larger deformation will have a larger area inside the force zone, while more stiff cells have a smaller area affected by the intersurface forces. Therefore, deposition should be the combination of energy interactions (depends on vertical distance between each point on cell surface and collector) and the effect of deformed cell shape. Modified Tabor's parameter quantifies the deposition behavior by integrating both the energy interactions (indicated by the overall adhesion energy measured with AFM) and the deformation (indicated by the cell size and elastic modulus). Note that the distances shown are for typical bacterial cells for illustration, while actual values vary depending on bacteria and surface.

Figure 4 illustrates the impact of cell deformation on the cell–surface interaction forces, which explains the underlying mechanism for the ability of proposed Tabor's parameter to predict cell attachment efficiency. Note that unlike model particles ( $\sim 10$  nm), microbial cells ( $2\text{--}5\ \mu\text{m}$ ) are usually much larger than the surface force range ( $100\text{--}500$  nm) and have elasticity. Only the localized area at the contact and a small surrounding cohesive zone can sense the interaction, which leads to local mechanical deformation. Away from the cohesive zone no surface force is felt. Consequently, the extent of cell deformation (which varies for different bacterial strains) affects the relative portion of the cell surface that is within the intersurface force zone. Thus, instead of using one single value for the whole cell, energy interactions should be considered as a function of the vertical distance between each point on the cell surface and sand surface. Therefore, deposition should be a combination of energy interactions and the effect of deformed cell shape. The modified Tabor parameter can more comprehensively present the deposition behavior by integrating both the energy interactions (indicated by the overall adhesion energy measured when pulling up the deposited cell from the surface) and the deformation (indicated by the cell size and elastic modulus). The fact that Tabor values seemed to be a good predictor for the deposition rate of a bacterium suggested that the AFM tests performed between a single-cell and a surface captured the key quantities of the interactions between the cell and the surface that dictate the overall cell transport and deposition behavior. Tabor's parameter therefore can be potentially incorporated into the microbial transport model.

## ■ ASSOCIATED CONTENT

### Supporting Information

Detailed discussion of AFM parameter computation and Tabor value derivation, DLVO calculations, and more figures

illustrating the cell aggregation diameter and AFM loading curves. This material is available free of charge via the Internet at <http://pubs.acs.org>.

## ■ AUTHOR INFORMATION

### Corresponding Author

\*E-mail: [april@coe.neu.edu](mailto:april@coe.neu.edu).

### Author Contributions

The first two coauthors contributed to the manuscript equally and can be considered as cofirst authors.

### Notes

The authors declare no competing financial interest.

## ■ ACKNOWLEDGMENTS

The authors acknowledge support from the Department of Energy's Environmental Remediation Science Program (DOE-SBR Grant no. DE-SC0005249), Northeastern University Tier 1 Research Grant, and National Science Foundation CMMI #1333889. We are grateful to Dr. Christopher Schadt at the U.S. DOE for providing the *Shewanella* and *Desulfovibrio* strains, Dr. Derek Lovely for providing *Geobacter* strain, and Dr. Yanru Yang at East Bay Municipal Utility District (formerly with Clemson University) for providing all other isolated strains.

## ■ REFERENCES

- (1) Steffan, R. J.; S., K. L.; Walsh, M. T.; Vainberg, S.; Condee, C. W. Field-scale evaluation of in situ bioaugmentation for remediation of chlorinated solvents in groundwater. *Environ. Sci. Technol.* **1999**, *33*, 2771–2781.
- (2) Ferguson, C.; Husman, A. M. d. R.; Altavilla, N.; Deere, D.; Ashbolt, N. Fate and Transport of Surface Water Pathogens in Watersheds. *Crit. Rev. Environ. Sci. Technol.* **2003**, *33* (3), 299–361.
- (3) Tufenkji, N.; R., J. N.; E., M. The promise of bank filtration. *Environ. Sci. Technol.* **2002**, *36*, 422–428.
- (4) Tobiason, J. E.; O'melia, C. R. Physicochemical aspects of particle removal in depth filtration. *J.—Am. Water Works Assoc.* **1988**, 54–64.
- (5) Battin, T.; Sengschmitt, D. Linking sediment biofilms, hydrodynamics, and river bed clogging: evidence from a large river. *Microb. Ecol.* **1999**, *37* (3), 185–196.
- (6) Pang, L.; Šimůnek, J. Evaluation of bacteria-facilitated cadmium transport in gravel columns using the HYDRUS colloid-facilitated solute transport model. *Water Resour. Res.* **2006**, *42*, W12S10.
- (7) Gerba, C. P. Microbial contamination of the subsurface. *Ground Water Quality*; John Wiley: New York, 1985; pp 53–67.
- (8) Elimelech, M.; Gregory, J.; Jia, X.; Williams, R. *Particle deposition and aggregation: measurement, modelling, and simulation*; Butterworth-Heinemann: Oxford, England, 1995.
- (9) Yates, M. V.; Yates, S. R.; Gerba, C. P. Modeling microbial fate in the subsurface environment. *Crit. Rev. Environ. Sci. Technol.* **1988**, *17* (4), 307–344.
- (10) Schijven, J. F.; Medema, G.; Vogelaar, A. J.; Hassanizadeh, S. M. Removal of microorganisms by deep well injection. *J. Contam. Hydrol.* **2000**, *44* (3–4), 301–327.
- (11) Ryan, J.; Elimelech, M. Colloid mobilization and transport in groundwater. *Colloids Surf, A* **1996**, *107*, 1–56.
- (12) Schijven, J.; Majid, H. Removal of Viruses by Soil Passage: Overview of Modeling, Processes, and Parameters. *Crit. Rev. Environ. Sci. Technol.* **2000**, *30* (1), 49–127.
- (13) Schijven, J.; Hoogenboezem, W.; Hassanizadeh, S. M.; Peters, J. H. Modeling removal of bacteriophages MS2 and PRD1 by dune recharge at Castricum, Netherlands. *Water Resour. Res.* **1999**, *35* (4), 1101–1111.
- (14) DeBorde, D. C.; Woessner, W. W.; Kiley, Q. T.; Ball, P. Rapid transport of viruses in a floodplain aquifer. *Water Res.* **1999**, *33* (10), 2229–2238.

- (15) Bales, R. C.; Li, S.; Yeh, T.-C. J.; Lenczewski, M. E.; Gerba, C. P. Bacteriophage and microsphere transport in saturated porous media: Forced-gradient experiment at Borden, Ontario. *Water Resour. Res.* **1997**, *33* (4), 639–648.
- (16) Bales, R. C.; S.L., K.; Maguire, M.; Yahya, M. T.; Gerba, C. P.; Harvey, R. W. Virus and Bacteria Transport in a Sandy Aquifer, Cape Cod, MA. *Ground Water* **1995**, *33* (4), 653–661.
- (17) Verwey, E. J. W.; Overbeek, J. T. G. *Theory of the Stability of Lyophobic Colloids*; Dover: New York, 1999.
- (18) Derjaguin, B.; Landau, L. Theory of the stability of strongly charged lyophobic sols and of the adhesion of strongly charged particles in solutions of electrolytes. *Acta Phys. Chem. URSS* **1941**, *14*, 633.
- (19) Redman, J.; Estes, M.; Grant, S. B. Resolving macroscale and microscale heterogeneity in virus filtration. *Colloids Surf., A* **2001**, *191* (1–2), 57–70.
- (20) Seitz, M.; Park, C. K.; Wong, J. Y.; Israelachvili, J. N. Long-range interaction forces between polymer-supported lipid bilayer membranes. *Langmuir* **2001**, *17*, 4616–4626.
- (21) van Loosdrecht, M. C.; Lyklema, J.; Norde, S.; Zehnder, A. J. Bacterial adhesion: A physicochemical approach. *Microb. Ecol.* **1989**, *17*, 1–15.
- (22) Rijnaarts, H. H. M.; Norde, W.; Lyklema, J.; Zehnder, A. J. B. DLVO and steric contributions to bacterial deposition in media of different ionic strengths. *Colloids Surf., B* **1999**, *14* (1–4), 179–195.
- (23) Van Loosdrecht, M.; Lyklema, J.; Norde, W.; Schraa, G.; Zehnder, A. Electrophoretic mobility and hydrophobicity as a measured to predict the initial steps of bacterial adhesion. *Appl. Environ. Microbiol.* **1987**, *53* (8), 1898.
- (24) Tufenkji, N.; Elimelech, M. Breakdown of colloid filtration theory: Role of the secondary energy minimum and surface charge heterogeneities. *Langmuir* **2005**, *21* (3), 841–852.
- (25) Walker, S. L.; Redman, J. A.; Elimelech, M. Role of Cell Surface Lipopolysaccharides in *Escherichia coli* K12 Adhesion and Transport. *Langmuir* **2004**, *20* (18), 7736–7746.
- (26) Bolster, C. H.; Cook, K. L.; Marcus, I. M.; Haznedaroglu, B. Z.; Walker, S. L. Correlating transport behavior with cell properties for eight porcine *Escherichia coli* isolates. *Environ. Sci. Technol.* **2010**, *44* (13), 5008–5014.
- (27) Tufenkji, N. Modeling microbial transport in porous media: Traditional approaches and recent developments. *Adv. Water Resour.* **2007**, *30* (6–7), 1455–1469.
- (28) Gaboriaud, F.; Dufrene, Y. F. Atomic force microscopy of microbial cells: Application to nanomechanical properties, surface forces and molecular recognition forces. *Colloids Surf., B* **2007**, *54* (1), 10–19.
- (29) Yao, X.; Walter, J.; Burke, S.; Stewart, S.; Jericho, M. H.; Pink, D.; Hunter, R.; Beveridge, T. J. Atomic force microscopy and theoretical considerations of surface properties and turgor pressures of bacteria. *Colloids Surf., B* **2002**, *23*, 213–230.
- (30) Xu, W.; Mulhern, P. J.; Blackford, B. L.; Jericho, M. H.; Firtel, M.; Beveridge, T. J. Modeling and measuring the elastic properties of an Archaeal surface, the sheath of *Methanospirillum hungatei*, and the implication for methane production. *J. Bacteriol.* **1996**, *178* (11), 3106–3112.
- (31) Zhao, L.; Schaefer, D.; Xu, H.; Modi, S. J.; LaCourse, W. R.; Marten, M. R. Elastic properties of the cell wall of *Aspergillus nidulans* studied with atomic force microscopy. *Biotechnol. Prog.* **2005**, *21*, 292–299.
- (32) Wang, X.; Li, Y.; Onnis-Hayden, A.; Gao, C.; Gu, A. Z.; Wan, K.-t. Correlation of macroscopic aggregation behavior and microscopic adhesion properties of bacteria strains using a dimensionless Tabor's parameter. *J. Colloid Interface Sci.* **2012**, *374* (1), 70–76.
- (33) Chandler, D. P.; Kukhtin, A.; Mokhiber, R.; Knickerbocker, C.; Ogles, D.; Rudy, G.; Golova, J.; Long, P.; Peacock, A. Monitoring microbial community structure and dynamics during in situ U (VI) bioremediation with a field-portable microarray analysis system. *Environ. Sci. Technol.* **2010**, *44* (14), 5516–5522.
- (34) Xu, M.; Wu, W. M.; Wu, L.; He, Z.; Van Nostrand, J. D.; Deng, Y.; Luo, J.; Carley, J.; Ginder-Vogel, M.; Gentry, T. J. Responses of microbial community functional structures to pilot-scale uranium in situ bioremediation. *ISME J.* **2010**, *4* (8), 1060–1070.
- (35) Yang, Y.; Chen, F.; Liu, X. A Redefinition of the Role of Microorganisms in Bioaggregation in Activated Sludge. *Proce. Water Environ. Fed.* **2007**, *2007* (18), 1422–1428.
- (36) Coppi, M. V.; Leang, C.; Sandler, S. J.; Lovley, D. R. Development of a Genetic System for *Geobacter sulfurreducens*. *Appl. Environ. Microbiol.* **2001**, *67* (7), 3180–3187.
- (37) Psenner, R. Determination of size and morphology of aquatic bacteria by automated image analysis. *Handbook of methods in aquatic microbiology*; Lewis Publishers: Boca Raton, FL, 1993; pp 339–346.
- (38) Van Loosdrecht, M.; Lyklema, J.; Norde, W.; Schraa, G.; Zehnder, A. The role of bacterial cell wall hydrophobicity in adhesion. *Appl. Environ. Microbiol.* **1987**, *53* (8), 1893–1897.
- (39) Park, C.; Novak, J. T. Characterization of activated sludge exocellular polymers using several cation-associated extraction methods. *Water Res.* **2007**, *41* (8), 1679–1688.
- (40) Dubois, M.; Gilles, K. A.; Hamilton, J. K.; Rebers, P.; Smith, F. Colorimetric method for determination of sugars and related substances. *Anal. Chem.* **1956**, *28* (3), 350–356.
- (41) Malik, A.; Kakii, K. Intergeneric coaggregations among Oligotropha carboxidovorans and Acinetobacter species present in activated sludge. *FEMS Microbiol. Lett* **2003**, *224* (1), 23–28.
- (42) Monier, J. M.; Lindow, S. Frequency, size, and localization of bacterial aggregates on bean leaf surfaces. *Appl. Environ. Microbiol.* **2004**, *70* (1), 346.
- (43) Bolster, C.; Haznedaroglu, B.; Walker, S. Diversity in Cell Properties and Transport Behavior among 12 Different Environmental Isolates. *J. Environ. Qual.* **2009**, *38* (2), 465–472.
- (44) Tufenkji, N.; Elimelech, M. Deviation from the classical colloid filtration theory in the presence of repulsive DLVO interactions. *Langmuir* **2004**, *20* (25), 10818–10828.
- (45) Tufenkji, N.; Elimelech, M. Correlation equation for predicting single-collector efficiency in physicochemical filtration in saturated porous media. *Environ. Sci. Technol.* **2004**, *38* (2), 529–536.
- (46) Kepner, R. L., Jr.; Pratt, J. R. Use of fluorochromes for direct enumeration of total bacteria in environmental samples: past and present. *Microbiol. Mol. Biol. Rev.* **1994**, *58* (4), 603.
- (47) Wang, X.; Shah, A. A.; Campbell, R. B.; Wan, K. T., Glycoprotein mucin molecular brush on cancer cell surface acting as mechanical barrier against drug delivery. *Appl. Phys. Lett.* **2010**, *97*, (26).
- (48) Cleveland, J.; Manne, S.; Bocek, D.; Hansma, P. A non-destructive method for determining the spring constant of cantilevers for scanning force microscopy. *Rev. Sci. Instrum.* **1993**, *64* (2), 403–405.
- (49) Camesano, T. A.; Unice, K. M.; Logan, B. E. Blocking and ripening of colloids in porous media and their implications for bacterial transport. *Colloids Surf., A: Physicochem. Eng. Aspects* **1999**, *160* (3), 291–307.
- (50) Meinders, J.; Noordmans, J.; Busscher, H. Simultaneous monitoring of the adsorption and desorption of colloidal particles during deposition in a parallel plate flow chamber. *J. Colloid Interface Sci.* **1992**, *152* (1), 265–280.
- (51) Haznedaroglu, B.; Kim, H.; Bradford, S.; Walker, S. Relative transport behavior of *Escherichia coli* O157: H7 and *Salmonella enterica* serovar pullorum in packed bed column systems: Influence of solution chemistry and cell concentration. *Environ. Sci. Technol.* **2009**, *43* (6), 1838–1844.
- (52) Bradford, S. A.; Yates, S. R.; Bettahar, M.; Simunek, J. Physical factors affecting the transport and fate of colloids in saturated porous media. *Water Resour. Res.* **2002**, *38* (12), 1327.
- (53) Redman, J. A.; Walker, S. L.; Elimelech, M. Bacterial adhesion and transport in porous media: Role of the secondary energy minimum. *Environ. Sci. Technol.* **2004**, *38* (6), 1777–1785.
- (54) Hahn, M. W.; O'Melia, C. R. Deposition and reentrainment of Brownian particles in porous media under unfavorable chemical

conditions: Some concepts and applications. *Environ. Sci. Technol.* **2004**, *38* (1), 210–220.

(55) Morisaki, H.; Nagai, S.; Ohshima, H.; Ikemoto, E.; Kogure, K. The effect of motility and cell-surface polymers on bacterial attachment. *Microbiology* **1999**, *145* (10), 2797–2802.

(56) Vogler, E. A. Structure and reactivity of water at biomaterial surfaces. *Adv. Colloid Interface Sci.* **1998**, *74* (1–3), 69–117.

(57) Foppen, J. W.; Lutterodt, G.; Roling, W. F. M.; Uhlenbrook, S. Towards understanding inter-strain attachment variations of *Escherichia coli* during transport in saturated quartz sand. *Water Res.* **2010**, *44* (4), 1202–1212.

(58) Abu-Lail, N. I.; Camesano, T. A. Role of lipopolysaccharides in the adhesion, retention, and transport of *Escherichia coli* JM109. *Environ. Sci. Technol.* **2003**, *37* (10), 2173–2183.

(59) Sakthivadivel, R. *Theory and mechanism of filtration of non-colloidal fines through a porous medium*; University of California: Berkeley, 1967.

(60) Maugis, D. *Contact, Adhesion and Rupture of Elastic Solids*; Springer: New York, 2000.

(61) Wan, K.-T.; Liu, K.-K. Contact mechanics of a thin-walled capsule adhered onto a rigid planar substrate. *Med. Biol. Eng. Comput.* **2001**, *39* (5), 605–608.

(62) Tabor, D. Surface forces and surface interactions. *J. Colloid Interface Sci.* **1977**, *58* (1), 2–13.